Astron. Astrophys. 357, 533–542 (2000)

ASTRONOMY AND ASTROPHYSICS

The Vega phenomenon around G dwarfs⋆

G. Decin[1], **C. Dominik**[2], **K. Malfait**[1], **M. Mayor**[3], **and C. Waelkens**[1]

[1] Instituut voor Sterrenkunde, KULeuven, Celestijnenlaan 200B, 3001 Leuven, Belgium
[2] Sterrenkundig Instituut 'Anton Pannekoek', Kruislaan 403, 1098 SJ Amsterdam, The Netherlands
[3] Observatoire de Genève, 1290 Sauverny, Switzerland

Received 16 December 1999 / Accepted 14 March 2000

Abstract. In this paper, we present and discuss photometric infrared measurements taken with ISOPHOT at 60 μm for a sample of 30 G dwarfs, using C100 3X3 minimaps. This sample was selected from the set of more than 1600 G dwarfs which will be scrutinized for radial-velocity variations by the Geneva group, aiming at the detection of extra-solar planets. In our sample, 5 stars display an infrared excess at 60 μm.

We have compared our results with those of Habing et al. (1999, in prep.), who have investigated the incidence and the survival of remnant disks around main-sequence stars. They concluded that most stars which arrive on the main-sequence still possess a disk, and that this disk then decays in the next 400 Myr. The 5 stars in our sample which have an infrared excess, are probably older than 3 Gyr, however, from which we suggest that the disks around cool stars may survive longer than those among earlier-type objects. For two stars in our sample, the fractional luminosity of the disk is significantly higher than for typical Vega-type stars, and approaches the exceptional value observed for β Pic.

To investigate the correlation between an infrared excess and planets/companion stars, we combine our results with the first results of the CORALIE survey. None of the until now detected radial-velocity variables display an infrared excess. That the stars for which an infrared excess is found lack a companion, can however not be concluded at the present stage.

Key words: stars: circumstellar matter – stars: individual: G dwarfs – stars: planetary systems – infrared: stars

1. Introduction

Since the IRAS space mission detected in 1983 an excess of infrared radiation for Vega (Aumann et al. 1984), Fomalhaut and β Pictoris (Gillett 1986), and since Smith & Terrile (1984) imaged the dust disk surrounding β Pictoris in the optical for the first time, the study of this so-called 'Vega phenomenon' has received a substantial amount of interest, opening new possibilities for studying other planetary systems than our own. The interest in planetary material around other stars received new stimuli with the detection of Jupiter-like planets around solar-type stars (Mayor & Queloz 1995; Marcy & Butler 1995, 1996).

It rapidly became clear that the dusty disk observed in Vega-like stars needs replenishment to survive, given the main-sequence ages of the stars which are much longer than the typical lifetimes of the circumstellar disks which accompany the star-formation process. This replenishment is widely attributed to collisions of small-size bodies, comets or planetesimals, and evaporation of larger bodies, which thus must still be present in the disks of Vega-like stars, suggesting that the process towards the formation of major planets was to some extent hampered in such systems. Moreover, the gravitational perturbations by giant planets are thought to remove a large fraction of the remaining dust, comets and planetesimals of the inner system on short timescales.

However, indirect indications exist that the β Pictoris system may harbour a planet (Roques et al. 1994; Lagage & Pantin 1994; Burrows et al. 1995). ISO spectroscopy shows that this might also be the case for evolved 'isolated' Herbig Ae/Be stars such as HD100546 (Malfait et al. 1998). Even stronger evidence is found in the case of ρ^1 Cancri, which is significantly older than the former objects. This object, classified as a G8V star, hosts a planet, detected from radial velocity measurements by Butler et al. (1997). In an ISOPHOT search for Vega-type systems, similar to the one described in this paper, Dominik et al. (1998) show that ρ^1 Cancri has a Vega-like dust excess. However, there might be no direct correlation between the planet around ρ^1 Cancri and the disk around this star. The planet around ρ^1 Cancri is too close to the star in comparison with the inner disk radius, so it does not affect the disk seen today. The presence of a disk can thus not simply be considered as a sign of failed planet formation.

Surveys for these phenomena indicate that both the presence of an infrared excess and the presence of planets, are not uncommon. In order to study the correlation or anti-correlation between the occurrence of observable dust debris disks and planets of Jupiter-like sizes in more detail, it is necessary to focus on

Send offprint requests to: G. Decin

⋆ Based on observations with ISO, an ESA project with instruments funded by ESA Member States (especially the PI countries: France, Germany, The Netherlands and the United Kingdom) and with the participation of ISAS and NASA

Correspondence to: G.Decin (greet@ster.kuleuven.ac.be)

Table 1. The stars of the sample

Nr	HD	Name	Spectral Type	B mag	V mag	π mas	d pc	$T_{\rm eff}$ K	log g	$[Fe/H]$
(1)	(2)	(3)	(4)	(5)	(6)	(7)	(8)	(9)	(10)	(11)
1	1002		G5V	7.10	6.46	20.23	49.43	5813	4.44	$+0.08$
2	1237		G6V	7.20	6.70	56.76	17.62	5504	5.06	-0.17
3	3823		G1V	6.44	5.88	39.26	25.47	6013	4.20	-0.33
4	10647	q1 Eri	F9V	6.05	5.52	57.63	17.35	6107	4.56	-0.15
5	12951		F8/G0V	7.40	6.80	21.86	27.13	6053^1	4.06^1	-0.26^1
6	13445		K1V	6.94	6.17	91.63	24.36	5072^2	4.56^3	-0.15^4
7	18907	ϵ For	G5IV	6.68	5.85	32.94	6.06	5471^5	4.41^6	-0.30^5
8	20407		G1V	7.35	6.77	41.05	47.06	5964	4.71	-0.38
9	20794	82 Eri	G8V	4.98	4.27	165.0	13.72	5537	4.83	-0.40
10	22166		F7V	7.20	6.70	21.25	23.19	6222	4.37	$+0.03$
11	22484	10 Tau	F9IV-V	4.86	4.28	72.89	41.56	5971	4.07	-0.16
12	26491		G3V	7.02	6.37	43.12	35.36	5787	4.07	-0.22
13	30606	59 Eri	F8V	6.32	5.75	24.06	18.21	6166	3.95	$+0.03$
14	36108		G3V	7.30	6.80	28.28	26.70	5912	4.45	-0.31
15	39091	π Men	G1V	6.25	5.67	55.92	16.69	6023	4.78	$+0.10$
16	41700		G0IV-V	6.87	6.35	37.46	22.04	6187	4.57	-0.13
17	43162		G5V	7.11	6.39	59.90	31.79	5593	4.69	-0.26
18	45701		G3III-IV	7.12	6.45	31.46	37.22	5782	4.45	$+0.04$
19	46569		F8V	6.14	5.60	26.87	26.60	6160	3.95	$+0.01$
20	48938		G2V	6.99	6.43	37.60	18.41	6016	4.11	-0.53
21	53143		K1V	7.61	6.81	54.33	17.76	5454	4.87	-0.02
22	165499	ι Pav	G0V	6.07	5.49	56.32	50.40	5887	4.25	-0.24
23	170525		G5IV	7.12	6.42	19.84	52.44	5556	4.04	-0.40
24	193307		G0V	6.82	6.28	30.84	17.71	5994	4.29	-0.35
25	196378	ψ2 Pav	F8V	5.65	5.12	41.33	32.43	6013	3.92	-0.44
26	204385		G0IV	7.80	7.20	25.55	24.20	5999	4.42	$+0.00$
27	210272		G3V	7.88	7.22	19.51	39.14	5629	4.25	-0.43
28	210918		G5V	6.88	6.26	45.19	51.26	5729	4.34	-0.27
29	214953		G0V	6.56	6.02	42.47	22.13	6051	4.38	-0.01
30	219077		G8V	6.91	6.12	34.29	23.55	5640^6	3.84^3	-0.40^7

1. Marsakov & Shevelev 1995 2. Favata et al. 1997 3. Using the mass- luminosity relation, the mass was determined. The gravity is calculated using the well-known formula: $\log g = \log M/M_\odot - \log L/L_\odot + 4 \log T_{\rm eff} - 10.606$ 4. Rocha-Pinto & Maciel 1998 5. Lebre et al. 1999 6. The effective temperature is derived from the spectral type. 7. Eggen 1987

a sample of objects for which both phenomena can be detected easily. The search for exosolar planetary systems from high-accuracy radial-velocity observations is most often carried out for slowly rotating G dwarfs, which present many narrow spectral lines, have a low intrinsic variability, and are sufficiently bright for high signal-to-noise observations. On the other hand, Habing et al. (in prep.) propose as a theorem that equal disks around A, F and G dwarfs have an equal probability of being detected, i.e. the stellar temperature does not affect the contrast, which is the ratio of the flux density of the disk at 60 μm to the photospheric flux density at 60 μm. This statement is not fully valid for K-stars since their remnant disks produce a somewhat lower contrast. Unfortunately stars of early spectral type have broader spectral lines, and so are not suitable for high-accuracy radial-velocity observations. G dwarfs are therefore the group of stars most suited for a correlated study of both phenomena.

Since late 1997, the Geneva group scrutinizes a sample of more than 1600 G dwarfs with the radial-velocity instrument CORALIE, mounted on the new Swiss Telescope operational at La Silla Observatory in Chile. We have undertaken a parallel search for circumstellar debris in a subsample of these G dwarfs with the ISOPHOT instrument on board the Infrared Space Observatory ISO (Kessler et al. 1996; Lemke et al. 1996). Considering that the emission of dust debris disks surrounding main-sequence stars usually peaks at 60 μm, we have opted for 60 μm ISOPHOT observations.

The plan of this paper is as follows: in the next section, we introduce the selected objects. In Sect. 3, the observations are described, as well as the data reduction. Sect. 4 is devoted to the observational results, and a more elaborate interpretation and discussion of these results is presented in Sect. 5.

2. The programme stars

2.1. Sample selection

The Geneva group had selected a large sample of G dwarfs on which accurate radial velocity measurements were carried out

with CORAVEL, aimed at determing the stellar duplicity of solar-stars (Udry et al. 1998). The northern CORAVEL spectrometer was mounted on the one-meter swiss telescope at the Haute-Provence Observatory (OHP) and produced stellar radial velocities at a rate of about 7500 measurements per year, with a precision of 300m s^{-1}. This CORAVEL sample of G dwarfs is largely included in the CORALIE planet-search programme. The CORALIE spectrometer is mounted on the Leonard Euler Swiss telescope at La Silla Observatory, having a precision of 10 m s^{-1}. The main difference between the CORAVEL and the CORALIE sample, is that the CORALIE sample was refined with the HIPPARCOS catalogue, i.e. it is based on distance criteria rather than photometric criteria as was the case for the CORAVEL G-dwarf sample. The CORALIE sample selection was performed according to the following criteria: (1) stars closer than 50 pc with $\sigma_\pi \leq 5$ mas and spectral type between F8 and M1 in the HIPPARCOS catalogue, (2) photometric cut-off of giant stars and (3) removal of faint cool dwarfs by a colour-dependent distance cut-off (Udry et al. 1999).

From the CORALIE sample of G dwarfs, we selected the southern objects in order to achieve complementarity with projects focussing on northern-hemisphere objects. A subsample of 100 G dwarfs were chosen from this subsample of southern stars according to the following criteria. First, the stars with a visual magnitude higher than 7.5 were rejected in order to optimize the signal-to-noise ratio of the results. A second criterion is, of course, the visibility by ISO (after the second call for proposals, i.e. after revolution 375). In the next step the stars affected by a high infrared background ($>$ 0.5 Jy/pixel) and cirrus ($>$ 0.04 Jy/pixel) were removed from the sample, as well as multiple systems and objects which overlap with other programmes. Finally, we picked the 60 μm brightest stars in order to increase the change of a detection. The photospheric flux of the fainter objects of our sample can be lower than 30 mJy, which is the sensitivity limit of ISOPHOT at this wavelength. For these faint objects, disks can thus only be found if the total flux at 60 μm exceeds the detection limit. The observing time that was recommended by the proposal refereeing committee enabled us to schedule observations of 69 stars, of which 34 could be observed before the ISO mission was completed.

2.2. Physical parameters of the programme stars

Table 1 contains those stars from our sample for which useful data were obtained. Four stars of the measured 34 G dwarfs were omitted, for reasons explained in section 3.1. In Table 1, columns 1, 2 and 3 contain a running number for each object, the corresponding HD number and, where it applies, the name. The spectral type and the Johnson B and V magnitude are tabulated in columns 4, 5 and 6. The Hipparcos parallax and the derived distance are listed in column 7 and 8 respectively.

The effective temperature $T_{\rm eff}$, the gravity g, and the metallicity $[Fe/H]$, are tabulated in columns 9, 10 and 11 respectively. The Geneva photometric system with the calibration by Künzli et al. (1997) was used to determine these parameters, except where indicated. The rms scatter of the differences between directly measured values of $T_{\rm eff}$ and the photometric value calculated from the Geneva photometric data amounts to 54 K, which is about 1%. The difference between the interpolated and fundamental $\log g$ values depends on the effective temperature and, especially for cool stars, on the metallicity. The rms scatter of the differences for $\log g$ is $\sigma = 0.15$ dex. The photometrically estimated surface gravities of cool stars are not so reliable as one would expect from the accuracy and homogeneity of the Geneva data. The most reliable values are those obtained for unevolved, solar-metallicity stars. The average rms scatter of the photometric $[M/H]$ and the fundamental $[Fe/H]$ amounts to $\sigma = 0.097$. For HD12951 no Geneva data were available, while HD13445, HD18907 and HD219077 were too cool and thus out of the validity range. The stellar parameters adopted for these stars were taken from the literature.

3. ISOPHOT Data

3.1. ISO observations

We have opted for a single ISOPHOT observation at 60 μm, considering the sensitivity of ISOPHOT and the fact that known dust debris disks emit their maximum near this wavelength. We first opted for the observation mode AOT PHT37, consisting of a C100 staring observation on source and four staring observations of the background around the target, making a sparse map. These observations turned out, however, not to be sufficiently reliable, because each sky position is measured only once with the same pixel, so that no flatfielding is possible. After 3 such observations (HD10800, HD177171 and HD189567), we switched to the observation mode AOT PHT22 and required 3X3 mini-maps with the C100 detector at 60 μm. The step size used was 46″, i.e. full pixel size and the integration time per rasterposition is 128s. The observation of HD45184 was omitted because of a solar flaring event during revolution 722. In total, a usable C100 mini-map reduction was thus performed for 30 G dwarfs.

3.2. Data reduction

Our data reduction has been performed with PIA v7p3(e) (PHT Interactive Analysis - Gabriel et al. 1997). Long-term responsivity drifts were modeled by determining the background baseline (eye-balling method). This baseline drift was subtracted from the signal average per chopper plateau (V s^{-1}).

Since there was no standard method to extract the flux from the mini-map observations, we have developed a method based on the point-spread function fractions related to the ISOPHOT C100 (Laureijs 1999). The fraction of the point-spread function falling on a C100 pixel, $f_{\rm psf}(d)$, with d the distance from the point source centred on an ISOPHOT camera pixel, has been determined per filter for a number of typical pointing configurations. The point-spread function fractions for pixels in the C100 array for the 60 μm filter are listed in Table 2.

Fig. 1 shows the orientation of the individual pixels with regard to the source for the different raster positions taken by the raster scan during the observation. The method is based on

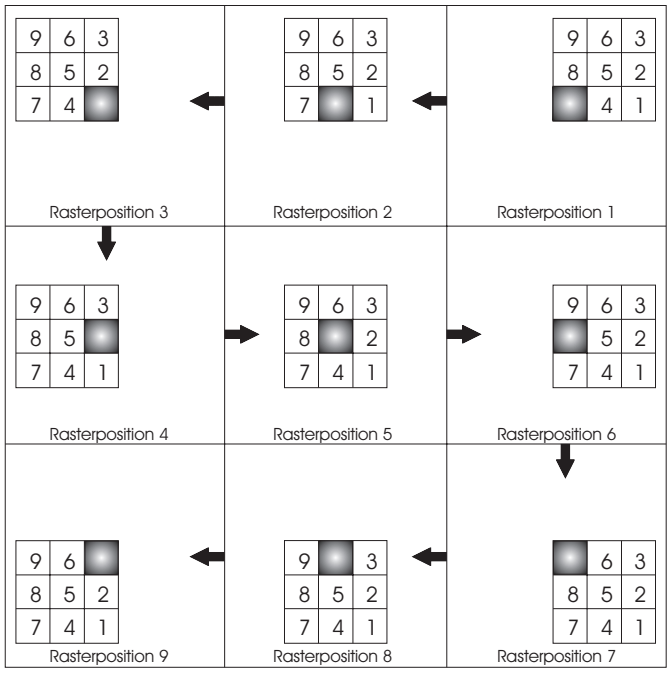

Fig. 1. The orientation of the pixels of the C100 detector with regard to the source for the different raster positions taken by the raster scan during the observation

Table 2. The measured point spread function fractions for pixels in the C100 array for the 60 μm filter (Laureijs 1999).

$f_{\rm psf}(0)$	0.69
$f_{\rm psf}(46'')$	0.0259±0.0021
$f_{\rm psf}(46\sqrt{2}'')$	0.0039±0.0003
$f_{\rm psf}(92'')$	0.0010±0.0004

the assumption that the point source is positioned in the centre of the mini-map. This means that it is implicitly assumed that the pointing accuracy is better than a few arcseconds so that flux variations due to pointing errors are negligible.

The result of a mini-map measurement is a flux per pixel for each pixel and each raster position. Let $F^*_\nu(p,r)$ be the measured flux in pixel p at raster position r (Jy/beam). The flux of the source is indicated by $F_{\nu,\rm src}$ and that of the background by $F_{\nu,\rm bck}$ (Jy). For each pixel p, and raster position r, the distance d(p,r), to the centre of the point source is determined using Fig. 1.

Because pixel 6 of the C100 camera shows a dark signal which is a factor 3–7 higher than for the other pixels in the C100 array, this pixel is omitted in further calculations (Laureijs et al. 1998).

First, the flatfield correction factors are calculated for each pixel (except pixel 6), $f_{\rm flat}(p)$. These flatfield corrections are at most 10% and are especially requisite for producing maps with extended structures. For point sources, this correction is in fact not necessary because the different pixel throughputs are corrected in the ISOPHOT photometric calibration by direct comparison with the calibration point sources. However, looking to the real data-set, the flatfield correction is recommended in order to obtain the same responsivity for each filter of the C100. The flatfield correction factors are calculated by assuming that

– the raster-position-averaged flux of pixels 1, 3, 7 and 9 is the same, as they cover a same area in the sky relative in distance to the source position, thus

$$f_{\rm flat}(p_i) = \frac{1}{4}\frac{\sum\limits_{p}\sum\limits_{r=1}^{9} F^*_\nu(p,r)}{\sum\limits_{r=1}^{9} F^*_\nu(p_i,r)},\quad p_i = 1,3,7,9, \tag{1}$$

where the summation over p is taken over the relevant pixels 1, 3, 7 and 9.

– the raster-position-averaged flux of pixels 2, 4 and 8 is the same thus

$$f_{\rm flat}(p_i) = \frac{1}{3}\frac{\sum\limits_{p}\sum\limits_{r=1}^{9} F^*_\nu(p,r)}{\sum\limits_{r=1}^{9} F^*_\nu(p_i,r)},\quad p_i = 2,4,8, \tag{2}$$

where the summation over p is taken over over the relevant pixels 2, 4 and 8.

– for each raster position r_i of pixel 5, the average of the flatfield corrected fluxes of the other pixels (except pixel 6) covering this sky position is the same. So if $f_{\rm flat}(5,r_i)$ indicates the flatfield correction factor for pixel 5 at raster position r_i then

$$f_{\rm flat}(5,r_i) = \frac{1}{n}\frac{\sum\limits_{p=p_i} f_{\rm flat}(p)F^*_\nu(p,r_x)}{F^*_\nu(5,r_i)}, \tag{3}$$

where n is the number of other pixels, p_i, covering this sky position and r_x chosen so that (p_i,r_x) is on the same sky position as (5,r_i). Thus the flatfield correction for pixel 5 is

$$f_{\rm flat}(5) = \frac{1}{9}\sum_{r_i=1}^{9} f_{\rm flat}(5,r_i). \tag{4}$$

Using this flatfield method, the pixels with similar 'distance history' to the source, thus with similar raster-position-averaged flux, get the same flatfielding. As a result, each group of pixels have internally consistent flatfielding, but are not necissarily flat with respect to each other. This might introduce a small error. If e.g. due to a glitch pixel 2 happens to be too high, then pixels 2,4 and 8 are affected and not pixels 1,3,7 and 9. However, if you do the flatfielding with all pixels together, the influence of the bad pixel will be of the same order of magnitude. The only way to do this entirely correct would be to have the full point spread function correction factors for each pixel in each position. Then it might be possible to design a procedure which gets the flatfield correct.

In the next step, the source flux and the background flux for each pixel p, and each raster position r, not on source, for

which $f_{\rm psf}(d)$ is known (the distance, d, dependent on p and r), is respectively computed from

$$F_{\nu,\rm src}(p,r) = \frac{F^*_\nu(p,r_0) - F^*_\nu(p,r)}{f_{\rm psf}(0) - f_{\rm psf}(d)}, \quad (5)$$

$$F^*_{\nu,\rm bck}(p,r) = \frac{f_{\rm psf}(0)F^*_\nu(p,r) - f_{\rm psf}(d)F^*_\nu(p,r_0)}{f_{\rm psf}(0) - f_{\rm psf}(d)}, \quad (6)$$

where r_0 is chosen so that (p,r_0) is on source and (p,r) is chosen so that $f_{\rm psf}(d)$ is known. Here, the flux for each pixel and each raster position is assumed to be flatfield corrected! The relative errors of the source flux and the background flux for these pixels on a certain raster position is respectively given by flux and background flux is

$$\frac{\sigma^2_{F_{\nu,\rm src}(p,r)}}{F^2_{\nu,\rm src}(p,r)} = \frac{\sigma^2_{F^*_\nu(p,r_0)} + \sigma^2_{F^*_\nu(p,r)}}{(F^*_\nu(p,r_0) - F^*_\nu(p,r))^2} + \frac{\sigma^2_{f_{\rm psf}(0)} + \sigma^2_{f_{\rm psf}(d)}}{(f_{\rm psf}(0) - f_{\rm psf}(d))^2} \quad (7)$$

and

$$\frac{\sigma^2_{F^*_{\nu,\rm bck}(p,r)}}{F^{*2}_{\nu,\rm bck}(p,r)} = \frac{F^{*2}_\nu(p,r)\sigma^2_{f_{\rm psf}(0)} + f^2_{\rm psf}(0)\sigma^2_{F^*_\nu(p,r)}}{(f_{\rm psf}(0)F^*_\nu(p,r) - f_{\rm psf}(d)F^*_\nu(p,r_0))^2} + \frac{F^{*2}_\nu(p,r_0)\sigma^2_{f_{\rm psf}(d)} + f^2_{\rm psf}(d)\sigma^2_{F^*_\nu(p,r_0)}}{(f_{\rm psf}(0)F^*_\nu(p,r) - f_{\rm psf}(d)F^*_\nu(p,r_0))^2} + \frac{\sigma^2_{f_{\rm psf}(0)} + \sigma^2_{f_{\rm psf}(d)}}{(f_{\rm psf}(0) - f_{\rm psf}(d))^2}. \quad (8)$$

The source flux and the background flux for each pixel $(F_{\nu,\rm src}(p), F^*_{\nu,\rm bck}(p))$, is calculated by the weighted mean of the source flux, respectively background flux, obtained for each raster position not on source for which $f_{\rm psf}(d)$ is known. The weighted mean is calculated by

$$\overline{X} = \sum_i w_i X_i / \sum_i w_i. \quad (9)$$

The minimal variance of $\overline{X}$

$$\sigma^2_{\overline{X}} = 1/\sum_k \sigma_k^{-2} \quad (10)$$

is obtained with the weights

$$w_i = \sigma_i^{-2} / \sum_k \sigma_k^{-2}. \quad (11)$$

In this context, $\overline{X}$ is $F_{\nu,\rm src}(p)$, respectively $F^*_{\nu,\rm bck}(p)$, X_i is $F_{\nu,\rm src}(p,r)$, respectively $F^*_{\nu,\rm bck}(p,r)$, $\sigma_{\overline{X}}$ is $\sigma_{F_{\nu,\rm src}(p)}$, respectively $\sigma_{F^*_{\nu,\rm bck}(p)}$ and σ_k is $\sigma_{F_{\nu,\rm src}(p,r)}$, respectively $\sigma_{F^*_{\nu,\rm bck}(p,r)}$. The sum over k is a summation over the relevant raster positions. The source and background flux $(F_{\nu,\rm src}, F^*_{\nu,\rm bck})$ are respectively calculated by taking the weighted mean of the source flux and the background flux, obtained for each pixel individually. We used Eq. (9), Eq. (10) and Eq. (11), but now $\overline{X}$ takes the values $F_{\nu,\rm src}$, respectively $F^*_{\nu,\rm bck}$, X_i is $F_{\nu,\rm src}(p)$, respectively $F^*_{\nu,\rm bck}(p)$, σ is $\sigma_{F_{\nu,\rm src}}$, respectively $\sigma_{F^*_{\nu,\rm bck}}$ and σ_k is $\sigma_{F_{\nu,\rm src}(p)}$, respectively $\sigma_{F^*_{\nu,\rm bck}(p)}$. The summation over k is over all pixels, except for pixel 6.

4. Results

4.1. Quality assessment of the results

4.1.1. Error due to incorrect background estimation

For accurate ISOPHOT measurements, care should be taken that the sky signal is of the same order of magnitude as the FCS (Fine Calibration Source) signal, but this condition was not satisfactorily met for our observations: the heating power of the FCS was too low and outside the 'soft' limits. Using such FCS measurements to determine the dectector responsivity can lead to a photometric bias larger than 15%, because an extrapolation of the FCS signal is necessary. Therefore, we decided to apply the default responsivity, which is a function of position along the orbit, and was determined by averaging many responsivity measurements along a revolution. It is thus implicitly assumed that the responsivity does not vary from one revolution to another. For the PHOT-SS, PHOT-SL, PHOT-P1, and PHOT-P2 detectors, this assumption can be considered to be valid within a few percent. The other detectors, PHOT-P3, PHOT-C100 and PHOT-C200, however, are more sensitive to space weather conditions. As a result, the default responsivities for a given observing date can be uncertain up to several tens of percent, which increases the systematical flux uncertainties (Laureijs & Klaas 1999).

4.1.2. Overall uncertainty

The statistical errors of our measurements are tabulated in Table 3, column 4, and are about 21%. In this kind of measurements the main systematical error comes from the dependence of the signal on (1) the error due to the reset interval length, which is decreased by a correction to less than 5%, (2) the error induced by the transient responsivity variation, which is also minimized by a correction to less than 5%, and (3) the use of default responsivities, which induces an error estimated as less than 20%. The fact that the default responsivities are used for observations at different revolutions of ISO adds enormously to the uncertainty, which is much larger than those of the flatfield and psf correction. The photometric bias consists of the error induced by the use of the default responsivities ($< 10\%$). This results in an overall error which may amount to some 30%. At the present stage of understanding of the instrument, there may still be some caveats in the ISOPHOT error budget calculation (Laureijs et al. 1999). Therefore, we decided to check the reliability of the end result not by analysing the overall uncertainties, but by performing some checks on the quality of the measured results by (1) comparing the measured fluxes with the predictions for the photosphere based on B- and V-photometry, (2) comparing the background fluxes with those measured by COBE/IRAS.

The quality of the results also depends on the pointing. We checked the correlation between the ISOPHOT pointing and the Hipparcos results and found that the difference between both is less than $4''$, except for HD20794 with a difference of $6''$ and HD22484 with a difference of $11''$, mainly in right ascension.

Table 3. Data results of the sample at 60 μm

Nr	HD	$F^{\rm PHT}_{\nu,\rm src}$	$\sigma_{F^{\rm PHT}_{\nu,\rm src}}$	$F^{\rm PHT}_{\nu,\rm bck}$	$\sigma_{F^{\rm PHT}_{\nu,\rm bck}}$	$F^{\rm pred}_{\nu,\rm src}$	PSC	fq	FSC	fq	$I^{\rm PHT}_{\nu,\rm bck}$	$I^{\rm COBE}_{\nu,\rm bck}$
		Jy	Jy	Jy	Jy	Jy	Jy	PSC	Jy	FSC	MJy/sr	MJy/sr
(1)	(2)	(3)	(4)	(5)	(6)	(7)	(8)	(9)	(10)	(11)	(12)	(13)
1	1002	-0.010	0.005	1.210	0.003	0.02					20.08	12.1
2	1237	+0.004	0.003	0.546	0.002	0.01	< 0.40	1			8.40	6.13
3	3823	+0.047	0.004	0.620	0.002	0.03					10.30	6.70
4	10647	+1.188	0.004	0.538	0.002	0.03	0.85	3			8.93	6.98
5	12951	+0.013	0.003	0.526	0.002	0.01	< 0.40	1	< 0.08	1	8.73	6.14
6	13445	+0.044	0.004	0.812	0.002	0.03	< 0.40	1	< 0.10	1	13.48	6.81
7	18907	+0.074	0.005	0.784	0.003	0.05	< 0.40	1	< 0.10	1	13.10	8.30
8	20407	+0.037	0.003	0.709	0.002	0.01	< 0.40	1			11.76	6.76
9	20794	+0.264	0.003	0.576	0.002	0.16	< 0.40	1	0.20	3	9.57	6.73
10	22166	-0.013	0.004	0.712	0.002	0.01	< 0.40	1			11.82	6.56
11	22484	+0.196	0.006	1.131	0.004	0.12	< 0.40	1	< 0.23	1	18.78	15.2
12	26491	+0.025	0.004	0.608	0.002	0.02	< 0.40	1			10.10	6.24
13	30606	+0.073	0.004	0.842	0.003	0.03	< 0.40	1			13.98	9.41
14	36108	+0.035	0.002	0.446	0.002	0.01	< 0.40	1	< 0.13	1	7.40	7.87
15	39091	+0.022	0.004	0.735	0.002	0.03	< 0.40	1			12.20	6.09
16	41700	+0.197	0.004	0.644	0.002	0.02	< 0.40	1	< 0.10	1	10.70	6.12
17	43162	-0.012	0.004	0.619	0.002	0.02	< 0.40	1	< 0.10	1	10.28	7.26
18	45701	-0.019	0.003	0.449	0.002	0.02	< 0.40	1			7.46	5.82
19	46569	+0.042	0.004	0.616	0.002	0.03	< 0.95	1	< 0.16	1	10.22	5.79
20	48938	+0.018	0.006	1.007	0.003	0.02	< 0.70	1	< 0.13	1	16.71	7.82
21	53143	+0.341	0.004	0.720	0.002	0.02	0.18	2	0.15	2	11.96	7.11
22	165499	+0.053	0.004	0.920	0.003	0.04	< 0.40	1			15.27	8.84
23	170525	+0.031	0.004	0.892	0.002	0.02	< 0.40	1			14.81	9.44
24	193307	+0.011	0.004	0.911	0.002	0.02	< 0.40	1	< 0.25	1	15.13	10.1
25	196378	+0.048	0.003	0.760	0.002	0.05	< 0.40	1	< 0.12	1	12.61	8.60
26	204385	+0.004	0.003	0.759	0.002	0.01					12.60	7.60
27	210272	+0.029	0.003	0.791	0.002	0.01					13.13	8.02
28	210918	+0.007	0.003	0.907	0.003	0.02	< 0.57	1	< 0.18	1	15.06	10.7
29	214953	+0.057	0.003	0.800	0.002	0.02	< 0.40	1	< 0.15	1	13.27	8.94
30	219077	+0.005	0.004	0.687	0.002	0.03	< 0.40	1	< 0.12	1	11.41	7.01

No quality check can be done by comparing the ISOPHOT results with those of IRAS, since most of the G dwarfs were too faint to be detected by IRAS. Almost all processed data of the G dwarfs in the IRAS Point Source Catalog (PSC) and Faint Source Catalog (FSC), which reaches about one magnitude fainter than the PSC, have upper limits only, namely fq equal to 1 (see Table 3 columns (8)-(11)).

We also checked the Hipparcos catalogue for variability and found a variation smaller than 0.05 mag in the Hipparcos photometric band at 0.6 μm for all stars. A five-percent variation of the photospheric flux at 60 μm for our sample of G dwarfs corresponds to an amplidtude smaller than 7.1 mJy, which is of the same order of magnitude as the statistical error. This variation is smaller then the errorbar determined in Sect. 4.2.

4.2. Results of the data reduction

More insight in the quality of the results is obtained by considering the histogram of the differences between measured, $F^{\rm PHT}_{\nu,\rm src}$, and predicted flux densities, $F^{\rm pred}_{\nu,\rm src}$, i.e the excesses, $F^{\rm exc}_{\nu,\rm src}$ (see Habing et al. 1999, in prep.). The predicted flux density, i.e the photosphere, is calculated using the equation derived by Plets (1997):

$$V-[12\,\mu m] = -0.03 + 2.99(B-V) \\ -1.06(B-V)^2 + 0.47(B-V)^3, \quad (12)$$

where [12 μm] is the stellar magnitude at 12 μm. To obtain the stellar magnitude at 60 μm, the color corrected IRAS color indices for a blackbody at 5000 K are used:

$$\left.\begin{array}{l} [12\,\mu m]-[25\,\mu m] = -0.007, \\ [25\,\mu m]-[60\,\mu m] = +0.034, \\ [60\,\mu m]-[100\,\mu m] = +0.150. \end{array}\right\} \quad (13)$$

The stellar magnitude [60 μm] can be converted into a flux density by:

$$f_\nu = K_\nu f_\nu[0.00\,mag]10^{-[60\,\mu m]/2.5}, \quad (14)$$

where f_ν[0.00 mag] is the observed flux density defining the zero magnitude of the photometric system at wavelength $\lambda = c/\nu$, being 1.19 Jy at 60 μm, and K_ν is the color correction

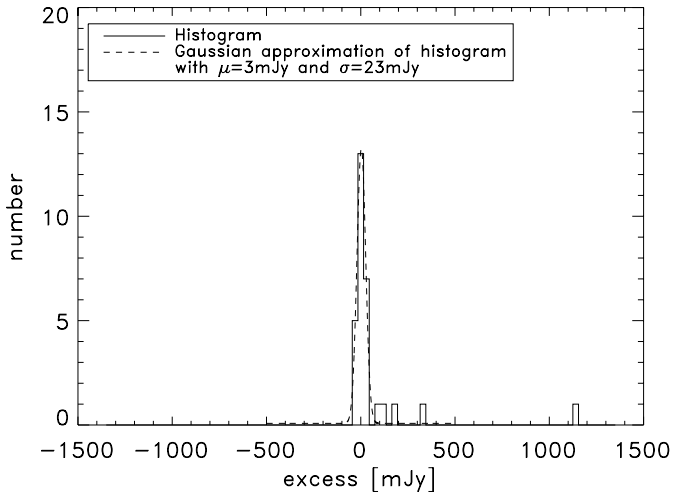

Fig. 2. Histogram of the differences between the measured flux density and the one predicted at 60 μm of our data sample

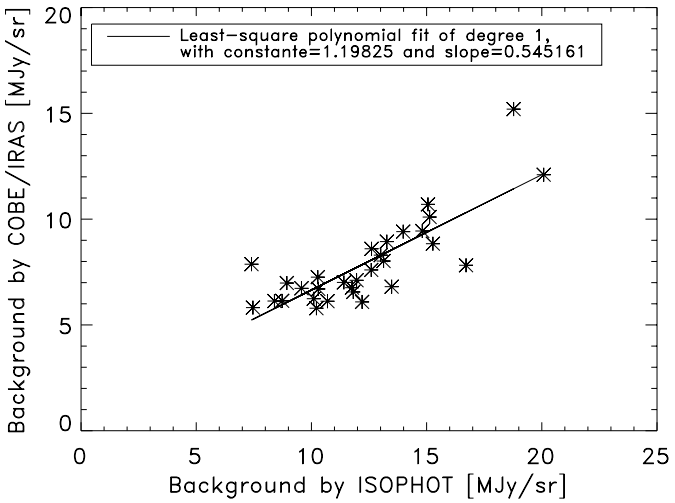

Fig. 3. Comparison between the background measured by ISOPHOT and those estimated by COBE/IRAS

factor, which is 1.32 for a blackbody at 5000 K for the 60 μm band. The results are tabulated in Table 3, column (7). Table 3 contains also some other parameters: in columns (3) and (4) the flux and its statistical error at 60 μm measured by ISOPHOT is tabulated ($F^{\rm PHT}_{\nu,{\rm src}}$, $\sigma_{F^{\rm PHT}_{\nu,{\rm src}}}$); columns (5) and (6) contain the background flux and its statistical error at 60 μm, measured by ISOPHOT ($F^{\rm PHT}_{\nu,{\rm bck}}$, $\sigma_{F^{\rm PHT}_{\nu,{\rm bck}}}$); in columns (12) and (13) the surface brightness of the background measured by ISOPHOT and by IRAS/COBE at 60 μm is listed ($I^{\rm PHT}_{\nu,{\rm bck}}$, $I^{\rm COBE}_{\nu,{\rm bck}}$).

In Fig. 2 the histogram of the excesses at 60 μm is shown. The distribution of the excess fluxes can be split into two components: a very narrow distribution around zero plus a wing of positive excesses, i.e. cases where we measure more flux than is produced by the stellar photosphere. A gaussian curve with average μ=3 mJy and dispersion σ=23 mJy is plotted on Fig 2. The value of σ confirms the estimate of the sensitivity of ISOPHOT at 60 μm we made in the previous subsection (30 mJy).

We conclude that a circumstellar disk is present when there is an excess at 60 μm amounting to more than μ+3σ=72 mJy. This criterion results in a list of 5 stars having an IR excess (see Table 4). Caution has to be taken with regard to the excess of HD22484, since the observation of this star was affected by a mispointing of 11 arcsec. The excess for this object is marginal in the framework of our excess criterion, and it is possible that the result is influenced by the strong background. We still accept the result, however, since for each pixel p, the maximum flux measured over all raster positions r is reached at the raster position when p points at the source.

The excesses found for HD10647 and HD53143 are confirmations of the results of surveys based on the IRAS database (Stencel & Backman 1991; Mannings & Barlow 1998). These two stars have the highest ISOPHOT IR excess. The other three excesses are new detections, these objects being too faint to be detected by IRAS.

HD214953 and HD10800 have been classified by Mannings & Barlow (1998) as stars with an infrared excess. The former object does not show any sign of an excess in our data, while the latter has been observed with an unsuitable observation mode, so no reliable ISOPHOT data are available for this source.

A quality check which has been mentioned above, is a comparison between the background measured by ISOPHOT with the background measured by COBE/IRAS (see columns (12) and (13) in Table 3). One sees from the table that the background flux estimated by ISOPHOT is systematically higher than that by COBE/IRAS. Fig. 3 reveals a clear correlation between both fluxes, namely

$$\mathrm{bckgr}_{\rm COBE/IRAS} = 1.2\,\mathrm{mJy/sr} + 0.5\ \mathrm{bckgr}_{\rm ISOPHOT}, \quad (15)$$

with σ=1.245 mJy/sr. The questions arise whether (1) this correlation is real or induced by a systematical error in one of the reduction steps, and whether (2) this correction has to be applied to the flux measurements on source. If this last statement is true, the amount of stars with an infrared excess at the 3-sigma level decreases to 3, i.e. those with the highest IR excesses. It looks suspicious that the stars in the sample with the highest photospheric fluxes show an excess emission. These stars (HD20794 and HD22484) are detected by ISOPHOT and a positive photometric calibration bias could probably cause the excess. This accidental correlation is however not alarming because most of the measured flux is dominated by the background. It is more important to investigate whether there exists a systematic trend between the total measured flux and the excess. However, there is a natural correlation between both because the excess is incorporated in the total flux. So a comparison between the background, which is most dominant in the total flux, and the excess is more significant. No correlation is revealed.

5. Discussion

5.1. Survival of the remnant dust disks

Column 3 of Table 4 contains the ages of the stars with an IR excess. We follow the criteria laid down by Lachaume et

Table 4. The excess stars at 60 μm

HD	values for $\log(age/1\,\mathrm{yr})$			method for	$F_{\nu,\mathrm{src}}^{\mathrm{PHT}}$	$F_{\nu,\mathrm{src}}^{\mathrm{pred}}$	$F_{\nu,\mathrm{src}}^{\mathrm{exc}}$	$\log(\tau_{60})$
	min	median	max	age determination				
					mJy	mJy	mJy	
(1)	(2)	(3)	(4)	(5)	(6)	(7)	(8)	(9)
10647	0.00	< 9.54	9.76	Isochrones	1188	34	1154	-3.27
20794	9.64	9.86	10.1	Calcium	264	156	108	-4.70
22484	9.66	9.72	9.77	Isochrones	196	118	78	-4.93
41700	0.00	< 9.63	9.65	Isochrones	197	15	182	-3.75
53143	8.81	8.99	9.17	Rotation + Calcium	341	18	323	-3.25

al. (1999) to choose the age estimator method. Isochrones provide the best results for stars with spectral type in the range B9-G5 (HD10647, HD22484 and HD41700). For HD22484, which is already evolved from the main-sequence (see Fig. 4), we used the age estimation of Lachaume et al. (1999). The ages of HD10647 and HD41700 are derived using the isochrones by Claret (Claret 1995; Claret & Gimenez 1995) with metallicity (X=0.73, Z=0.01) and (X=0.70, Z=0.02). For both metallicities, the age is determined by searching the isochrone which crosses the position of the object in the HR diagram. The effective age is calculated by a linear interpolation between the ages derived from these models, using the metallicity of the star. For HD41700 only the model with lower metallicity could be used the determine the age, since for the model with higher metallicity, the star is at the left of the ZAMS: only an upper-limit of the age is thus available. For both models, the maximum age is computed by searching the isochrone with maximal age in the rectangle ($M_v \pm \sigma_{M_v}, T_{\mathrm{eff}} \pm \sigma_{T_{\mathrm{eff}}}$). A linear interpolation between both determines the maximum age of the star. No precise estimate of the minimal age of these two stars could be made, since both are on the ZAMS within the uncertainties (see Fig. 4).

For stars redder than B-V=0.6 (corresponding to spectral type G1-2V), the rotation and the calcium emission lines method (see Lachaume et al. 1999) provide a good age estimation. For HD20794, a G8V star, only calcium emission lines are available. For HD53143, a K1V star, the age determined by the rotation period is 9.02 ± 0.14, the one determined by the calcium emission lines method is 8.96 ± 0.22. The average of both is indicated. Also for HD41700, calcium emission lines are available. The age amounts 8.11 ± 0.22, which is lower than the one determined by the isochrone method. Caution has to be taken with this age estimation because (B-V) is a little lower than 0.6.

In our sample, 17% of the stars occur with an IR excess, which is in good agreement with the fraction of main-sequence stars displaying the Vega phenomenon, 13 ± 10% (Plets & Vynckier 1999). Habing et al. (1999, in prep.) found that 60% of the main-sequence stars with spectral classes between A and K and younger than 400 Myr have a disk, but only 8% of those older than 400 Myr. From their survey they conclude that the A stars in general still possess a disk upon their arrival on the main-sequence, and that these disks are dispersed within about 400 Myr. They suggest that also the disks around F, G, and K stars decay in a similarly short time after arrival on the main

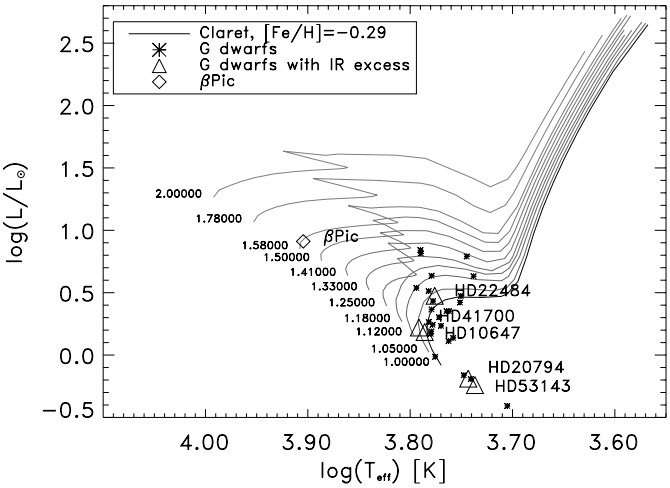

Fig. 4. The evolution tracks of Claret & Gimenez (1995) for X=0.7, Z=0.01 and mass between $1M_{\odot}$ and $2M_{\odot}$, together with the position of the G dwarfs

sequence. On the other hand, our stars are most likely older than 3 Gyr, and still 17% display an IR excess at 60 μm. Also HD207129, a G2V star, and ρ^1 Cancri, a G8V star, are surrounded by a disk and are older than 3 Gyr (Jourdain de Muizon et al. 1999; Dominik et al. 1998). It is currently unclear why the time scale of the removal of colliding planetesimals around these old G dwarfs is longer than for most other stars with a disk. Remarkable is that the time scale that corresponds to the dispersal of disks around G dwarfs is of the same order of magnitude as the time scale in which the disk around the Sun disappeared ($<$1 Gyr).

However, if the correlation between the background measured by ISOPHOT and by COBE/IRAS is correct and a correction has to be applied (see Sect. 4.2), the amount of G dwarfs displaying the Vega-phenomenon decreases to 10%, which is close to the 8% found for the stars, older than 400 Myr and having an infrared excess, in the sample of Habing et al. (1999, in prep.). In that case, our results fit well with the results from their survey.

5.2. Fractional luminosity

When considering an astrophysical phenomenon, one should always be aware that selection effects can bias the result. The

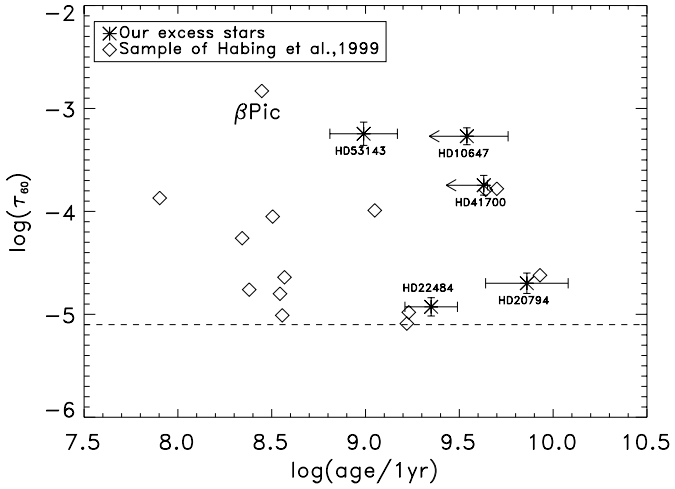

Fig. 5. Fractional luminosities as a function of the stellar age

infrared excess is believed to be caused by thermal emission of dust particles in a disk around the star. Thus, by attributing circumstellar disks to stars with an infrared excess, we might be selecting only the hottest disks, or, alternatively, the ones surrounding the hottest main-sequence stars. In order to take this selection effect into account, Backman & Gillett (1987) introduced a property which is independent of the stellar characteristics, namely the fractional luminosity τ, which is defined as

$$\tau \equiv F_{\rm bol}^{\rm exc}/F_{\rm bol}^{\rm photosp} = L^{\rm dust}/L^{\rm bol}. \quad (16)$$

This parameter is linked with the mass of the disk and can be estimated from observations (see Habing et al. in prep.).

On Fig. 5 the fractional luminosity, τ_{60}, derived from the 60 μm data, is plotted with respect to the stellar age, as well for our sample as for the sample of Habing et al. (in prep.). The lower limit at about $\tau = 10^{-5.1}$ occurs because ISOPHOT's sensivity limit does not allow the detection of fainter disks, comprising the zodiacal dust disk surrounding our Sun. In the sample of Habing et al. (in prep.), β Pic was an exception by having a value of τ of more than 10^{-3}. In this sample, ρ^1 Cancri and HD207129 have the largest fractional luminosity, respectively -3.78 and -3.79, which is near the fractional luminosity of HD41700. Several explanations for β Pic were proposed. First of all, the star may not yet have arrived on the main sequence (pre-main-sequence stars have disks with considerably more mass). Also possible is that a small fraction of main-sequence stars are born with much more massive disks than others, and β Pic might be the youngest among those. The fractional luminosity of HD10647 and HD53143 fills the gap between β Pic and the sample of Habing et al. (in prep.). Both stars are located at approximately the same distance as β Pic, but are cooler, less massive and older. In Fig. 4 we locate these stars on the evolution tracks by Claret & Gimenez (1995) with X=0.7 and Z=0.01. HD10647 and HD53143 appear to be true main-sequence stars and thus do not support the suggestion that massive disks only appear around pre-main-sequence stars. Note that β Pic is at this moment the only 'warm' main-sequence star known with such a high fractional luminosity.

Again, these results have to be evaluated against the hypothesis that Eq. 15 affects our conclusions. Beside the fact that the amount of stars with an infrared excess would then decrease, their fractional luminosities would decrease as well. For HD10647, HD41700 and HD53143 the logarithm of the fractional luminosity would be lowered to -3.54, -4.03 and -3.53, respectively. The highest values put these stars still in the gap between β Pic and the sample of Habing et al. (1999, in prep.), but the discrepancy is less marked.

5.3. Co-existence of a companion star or planet with a circumstellar dust disk: first results

The goal of this survey was to initiate an investigation of the (anti-)correlation between the presence of an infrared excess and the occurrence of planets or companion stars. Our sample is included in the CORALIE survey, which started recently. The following stars of our sample have already been detected as being double: HD1002, HD13445 (Gl86), HD22166, HD26491, HD45701, HD165499 and HD214953 (M. Mayor, private communication). HD10800 and HD177171, which were rejected from our sample because of a bad observation mode, were also detected as double. HD196378 is classified as an unconfirmed and doubtful double object (Kurster et al. 1997, 1999). None of these stars has a 60 μm infrared excess (except perhaps HD10800, see Sect. 4.2). For the other stars the results of the CORALIE survey are still not known. At the present stage, no clear correlation is found between dust disks and planets from our sample. However, based on the limited sample on which both phenomena have already been investigated, the conclusion that one phenomena prohibits the presence of the other one would be premature. A scenario in which a planet is located close to the central object, not affecting that part of the circumstellar dust disk located further out, is no wishful thinking. The completion of the CORALIE survey will hopefully provide more definitive results.

Acknowledgements. The ISOPHOT data presented in this paper was reduced using PIA, which is a joint development by the ESA Astrophysics Division and the ISOPHOT consortium. GD is supported by project IUAP P4/05 financed by the Belgian Federal Scientific Services (DWTC/SSTC). K.M is Postdoctoral Fellow of the Fund for Scientific Research - Flanders (Belgium) (F.W.O.).

References

Aumann H., Gillett F., Beichman C., et al., 1984, ApJ 278, L23
Backman D.E., Gillett F.C., 1987, In: Linsky J., Stencel R.E. (eds.) Cool Stars, Stellar Systems and the Sun, Springer-Verlag, Berlin, p. 340
Burrows C.J., Krist J.E., Stapelfeldt K.R., et al., 1995, American Astron. Soc. Meeting 187, 32.05
Butler R. P., Marcy G.W., Williams E., et al., 1997, ApJ 474, L115
Claret A., 1995, A&AS 109, 441
Claret A., Gimenez A., 1995, A&AS 114, 549

Dominik C., Laureijs R.J., Jourdain de Muizon M., et al., 1998, A&A 329, L53
Eggen O.J., 1987, AJ 92, 393
Favata F., Micela G., Sciortino S., 1997, A&A 322, 131
Gabriel C., Acosta-Pulido J., Heinrichsen I., et al., 1997, In: Hunt, G., Payne, H.E. (eds) proc. of the ADASS VI Conference, 108
Gillett F., 1986, In: Israel, F. (ed.) Light on dark matter, Reidel, Dordrecht, 61
Habing H.J., Dominik C., Jourdain de Muizon M., et al., 1999, Nat 401, 456
Jourdain de Muizon M., Laureijs R.J., Dominik C., et al., 1999, A&A 350, 875
Kessler M., Steinz J., Anderegg M., et al., 1996, A&A 315, L27
Künzli M., North P., Kurucz R.L., et al., 1997, A&AS 122, 51
Kurster M., Hatzes A., Cochran W.D., et al., 1997, In: Barbuy, B. (ed.) Proceeding Workshop Science with Gemini, Florianopolis, Brazil, December 7–10, in press
Kurster M., Hatzes A., Cochran W.D., et al., 1999, In: Hearnshaw, J.B., Scarfe, C.D. (eds.) Proceedings of IAU Colloquium 170, Precise stellar radial velocities, Victoria BC, Canada, in press
Lachaume R., Dominik C., Lanz T., et al., 1999, A&A 348, 897
Lagage P.O., Pantin E., 1994, Nat 369, 628
Laureijs R.J., 1999, Point spread function fractions related to the ISOPHOT C100 and C200 arrays
Laureijs R.J., Klaa, U., 1999, ISOPHOT error budgets: derive SPD processing steps
Laureijs R.J., Klaas U., Richards P.J., et al., 1998, ISOPHOT Data Users Manual
Lebre A., De Laverny P., De Medeiros J.R., et al., 1999, A&A 345, 936
Lemk, D., Klaas U., Abolins J., et al., 1996, A&A 315, L64
Malfait K., Waelkens C., Waters L.B.F.M, et al., 1998, A&A 332, L28
Mannings V., Barlow J.M., 1998, ApJ 497, 330
Marcy G.W., Butler R.P., 1995, Am. Astron. Society Meeting 175, 70.04
Marcy G.W., Butler R.P., 1996, ApJ 464, L153
Marsakov V.A., Shevelev Y.G., 1995, Bull. Inf. Centre Donees Stellaires 47, 13
Mayor M., Queloz D., 1995, Nat 378, 355
Plets H., 1997, Ph.D. Thesis, Katholieke Universiteit Leuven, België
Plets H., Vynckier C., 1999, A&A 343, 496
Rocha-Pinto H.J., Maciel W.J., 1998, MNRAS 298, 332
Roques F., Scholl H., Sicardy B., et al., 1994, Icarus 108, 37
Smith B.A., Terrile R.J., 1984, Sci 226, 1421
Stencel R.E., Backman D.E., 1991, ApJS 75, 905
Udry S., Mayor M., Latham D.W., et al., 1998, In: Donahue, R.A., Bookbinder, J.A. (eds.) Cool Stars, Stellar Systems and the Sun, 2148
Udry S., Mayor M., Queloz D., et al., 1999, paper presented at VLT Opening Symposium, Antofagasta, March 1–4, 1999